



Cite this: *Catal. Sci. Technol.*, 2016,
6, 7101

Plasmon-enhanced strong visible light photocatalysis by defect engineered CVD graphene and graphene oxide physically functionalized with Au nanoparticles†

Ravi K. Biroju,^{‡a} Biswajit Choudhury^{§b} and P. K. Giri^{*ab}

The strong visible light photocatalytic activity of defect-controlled CVD graphene (GR) and graphene oxide (GO) hybrids through physical functionalization with Au atoms has been demonstrated here. Control of in-plane defects in GR was achieved by controlling the pre-treatment of substrates during the CVD reaction, and post-growth functionalization was achieved using a physical sputter deposition approach. Quantitative analysis of the defect density, oxygenated functional groups on GR and nature of the interaction of Au with GR and GO was performed using several analytical tools. The defect-mediated strong interaction of the Au NPs with GR and GO and enhanced visible absorption was evidenced from surface plasmon resonance and surface-enhanced Raman spectroscopy studies. As compared to the pristine GR with a photocatalytic efficiency of ~30%, Au-functionalized defective GR and GO films exhibited catalytic efficiencies of 70% and 85%, respectively, for the first time. The pseudo first-order rate constant of degradation with visible light was found to be $\sim 10^{-3} \text{ min}^{-1}$. This is believed to result from the superior charge transfer in graphene-based plasmonic hybrids aided by enhanced light absorption. Our results open up doors for the efficient visible light photocatalysis and photoelectrocatalysis applications of graphene-based 2D layered materials.

Received 14th April 2016,
Accepted 24th July 2016

DOI: 10.1039/c6cy00826g

www.rsc.org/catalysis

1. Introduction

Environmental and water pollution are serious challenges faced by humanity today and effective removal of organic pollutants from water is essential for better and safe living. This calls for the development of new materials and new approaches, which may provide clean water and a sustainable environment and enable the conservation of renewable energy sources.¹ The degradation of organic pollutants using solar irradiation is the most attractive approach in wastewater treatment.² Wide varieties of semiconductor photocatalysts have been developed since the last few decades for practical and commercial applications.^{3,4} When these semiconductors are irradiated with light of photon energy higher or equal to their

band gaps, electrons in the valence band can be promoted to the conduction band, generating the same amount of holes in the valence band.⁵ The photogenerated electrons and holes can be trapped, generally by the oxygen and surface hydroxyls, to ultimately produce oxygen ($\text{O}_2^{\cdot-}$) and hydroxyl radicals ($\cdot\text{OH}$) that play vital roles in photocatalytic reactions.⁵ However, fast recombination of the photogenerated electrons and holes by defect centres can reduce the photocatalytic efficiency, limiting the applications of semiconductors in photocatalytic applications.

Among others, nanostructures of wide band gap semiconductors such as TiO_2 , ZnO, and ZnS have been extensively studied for photocatalytic applications.^{4,6-8} Among these, TiO_2 is most commonly used for photocatalytic applications because of its chemical stability, low toxicity, low cost and earth abundance.⁹ However, these kinds of photocatalysts are usually efficient in the UV region due to their near band edge optical absorption (band gap) at $\sim 3.3 \text{ eV}$. Interestingly, only 3% of UV light and 44% of visible light are present in the ground level sunlight spectrum, which means that TiO_2 -based materials are disadvantageous for utilization of the large amount of visible light in the solar spectrum. Recently, TiO_2 -based functional nanomaterials with plasmonic nanoparticles (NPs) and graphene have been developed to enhance visible light absorption for efficient hybrid

^a Centre for Nanotechnology, Indian Institute of Technology Guwahati, Guwahati 781039, India. E-mail: giri@iitg.ernet.in; Tel: +91 361 2582703

^b Department of Physics, Indian Institute of Technology Guwahati, Guwahati 781039, India

† Electronic supplementary information (ESI) available. See DOI: 10.1039/c6cy00826g

‡ Present address: TIFR-Center for Interdisciplinary Sciences, Tata Institute of Fundamental Research, 21-Brundavan Colony, Narsingi, Hyderabad-500075, Telangana State, India.

§ Present address: Institute of Advanced Study in Science and Technology (IASST), Paschim Borigaon, Guwahati 781035, Assam, India.

photocatalysts.^{10–15} In the semiconductor–metal NP hybrids, photoexcited electrons in the conduction band can be transferred to the plasmonic NPs, which act as a Schottky barrier at the metal–semiconductor interface, while the holes can remain on the semiconductor surface.^{16,17} The recombination of electrons and holes can be prolonged, and the photocatalytic efficiency will be improved.¹⁸ In addition, when more photons are absorbed due to the surface plasmon resonance (SPR) from plasmonic NPs, the photocatalytic efficiency of the semiconductors will be enhanced.¹⁹

In this regard, graphene and related semiconductor 2D nanomaterials and their plasmonic hybrid photocatalysts offer a new perspective for visible light photocatalysis and water purification for the present and the future.^{20–26} The primary goal for efficient visible light photocatalysis from new photocatalyst materials is to utilize the wide range of visible light absorption to generate large number of photogenerated electron–hole pairs and reduce the fast recombination of the photogenerated carriers during visible light irradiation. Apart from the conventional semiconductor photocatalysts, 2D nanomaterials have unique properties which can improve the photocatalytic efficiency. Among these, the intrinsic advantages of 2D materials that can be utilized to enhance photocatalytic efficiency are the large surface area per amount of material and the 2D nature of these materials that minimizes the distance that photogenerated electrons and holes migrate before reaching the solid/water interface, which reduce the possibility of recombination of electron–hole pairs and potentially enhance the photocatalytic performance.²¹ In this respect, graphene and related 2D nanomaterials present a new class of materials that display a wide range of electronic, optical, and mechanical properties.²⁷ There are unlimited possibilities to explore the interesting properties of graphene-based 2D nanomaterials and its hybrids with a diverse range of applications, including photocatalysis.^{28,29} On the other hand, numerous 2D nanomaterials can be fabricated from simple techniques (mechanical exfoliation and chemical synthesis) from bulk crystals or growth by chemical vapour deposition (CVD) or other thin-film growth methods,^{30–33} which makes them attractive candidates for investigation of their photocatalytic activity. However, due to the lack of band gap in graphene, graphene oxide-based plasmonic NP hybrids have been developed for direct application in enhanced visible light photocatalysis.^{25,34–38} There are very few reports on the selectivity and mechanism of visible light photocatalysts in these kinds of 2D plasmonic NP hybrids.³⁴ Most of these reports have focused on the UV light photocatalysis of GO-based hybrid materials and the functionalization has been performed by chemical methods. Zhang *et al.* reported the visible light photocatalytic activity of a Au–Pd/GO hybrid system fabricated using a chemical approach.²⁵ To the best of our knowledge, the visible light photocatalytic activity of defective graphene and GRAu hybrids through physical functionalization has not been reported yet. In particular, the explicit role of structural defects and functional groups in efficient visible light photocatalysis has not been studied sys-

tematically. It is believed that a nearly covalent linkage between graphene/GO and plasmonic NPs is possible using a physical functionalization technique and it may exhibit improved efficiency in visible light photocatalysis.³²

In the current work, we demonstrate the markedly improved visible light photocatalytic activity from physically functionalized CVD graphene (GR) and graphene oxide (GO) sheets with Au NPs by the photodegradation of methylene blue (MB) in solution. Particularly, the role of intrinsic and oxygenated functional group defects in the enhanced visible light photodegradation of MB was probed using micro-Raman, HRTEM and UV-visible absorption studies. Defective GR and GOAu plasmonic hybrids were found to display significantly improved photocatalytic activity over pristine samples. The origin of the enhanced photocatalytic activity has been thoroughly studied by degradation of MB to probe energy or electron transfer processes occurring at the defect sites/functional groups of the graphene and Au interface.

2. Experimental

2.1. Preparation of graphene and graphene oxide

We synthesized monolayer and few layer graphene by catalytic chemical vapour deposition (CVD) technique on a Cu foil of 25 μm thickness (purity 99.8%; Alfa-Aesar). Complete experimental details on the CVD growth of graphene and its wet transfer onto alien substrates are described in the ESI,† SI1 and SI2. Graphene oxide (GO) was synthesized by the modified Hummers method (see the ESI,† SI3) and then dispersed in a polar organic solvent (dimethylformamide (DMF)); subsequently high-quality GO film was fabricated on quartz and Si/SiO₂ substrates.³⁹

2.2. Physical functionalization of graphene by Au film

An ultra-thin Au film was deposited on the graphene layer by a radio frequency (RF) magnetron sputtering process under an Ar gas atmosphere with a RF power of <5 W. Au film was deposited in a controlled manner for 30 s at a deposition rate of 0.8 \AA s^{-1} . Au film was coated on the GR and GO deposited on Si/SiO₂, quartz and suspended graphene on a TEM Cu grid. Note that a high-purity sputter target (99.999%, diameter 2 inches, custom made) was used for the sputter deposition.

2.3. Rapid thermal annealing of graphene–Au hybrid films

The Au deposited graphene substrates were subjected to rapid thermal annealing (RTA) in order to form an array of Au nanoparticles (NPs) over the large area graphene. The RTA treatment was performed on the GR/Au, GO/Au hybrids present on the SiO₂, quartz and TEM Cu grid. Note that the RTA temperature was maintained at 600 °C for 3 min under a controlled flow of high-purity Ar gas. The average size of the Au NPs was found to be ~20 nm after RTA and 600 °C is found to be the optimum temperature for the NP growth. Note that

we did not observe any reduction/deoxygenation of GO samples after RTA treatment. In order to confirm the thermal stability of the GO films, we performed thermogravimetry (TGA) and XPS measurements (data not shown) and found no significant change in the microstructure and composition of the samples, particularly the functionalization and sp^2/sp^3 hybridization conditions. TGA measurements reveal that the GO is thermally stable up to ~ 700 °C. Thus, it is believed that GO films are highly stable after RTA treatment at 600 °C. TGA results of GO samples can be found elsewhere.³⁶ The Au-functionalized GR, DGR and GO catalysts were used to perform the photocatalysis experiment with visible light illumination. Details of the samples are presented in Table 1.

2.4. Visible light photocatalytic activity

The photocatalytic activities of pristine and Au-functionalized GR and GO plasmonic hybrids were assessed from the photocatalytic degradation of MB dye as the reference pollutant. MB solution with an initial concentration of 10 mg L^{-1} was prepared in 100 mL of distilled water. Thin films of pristine and GRAu plasmonic hybrids on quartz and Si/SiO₂ substrates were prepared and dipped into the MB dye solution and kept in the dark for 2 h to equilibrate the adsorption and desorption of dyes on the surface of the film. This film-dye solution was kept under visible light irradiation up to 120 min using a Xe lamp with a power of 250 W. After every 15 min of exposure, 5 mL of the irradiated dye solution was taken out and used for the absorption measurement. The photodegradation of MB was monitored by observing the changes in the maximum absorbance of MB at 664 nm. During the visible light irradiation on the catalyst substrates, the substrates were submerged in the dye solution and were continuously stirred by a magnetic stirrer underneath the beaker. More details of the photocatalysis experiment are presented later.

3. Characterization

The morphology and crystal structure of pristine CVD graphene, GO and Au-functionalized graphene were primarily characterized by high-resolution transmission electron microscopy (HRTEM) and micro-Raman spectroscopy. Raman measurements were performed with a high-resolution commercial spectrometer (Horiba, LabRam HR) with excitation wavelengths (λ_{ex}) of 514.5 nm (Ar ion laser) and 632.8 nm (He-Ne laser). The excitation source was focused using a

100× objective lens (spot size 2 μm , laser power 1 mW) to avoid laser heating and damage to the sample, and the signal was collected by a CCD in a backscattering geometry sent through a multimode fibre grating of 1800 grooves per mm. HRTEM measurements were conducted using a JEOL 2100 TEM operating at 200 kV. The UV-vis-NIR absorption spectroscopy measurements were recorded using a commercial spectrophotometer (Perkin Elmer). Fourier transform infrared spectroscopy (FTIR) measurements were carried out using a commercial FTIR spectrometer (Perkin Elmer, Spectrum BX) with KBr as a reference.

4. Results and discussion

4.1. Micro-Raman and Raman mapping studies

The physical functionalization of GR, DGR and GO with Au NPs is demonstrated by the evolution of characteristic Raman features through line shape analysis. The representative Raman fingerprints of pristine and Au-functionalized GR, DGR and GO are shown in Fig. 1(a)–(c), respectively. The structural change in each sample was estimated from the Lorentzian line shape fitting of the Raman spectral features. The important characteristic Raman features, namely D ($\sim 1350 \text{ cm}^{-1}$), G ($\sim 1580 \text{ cm}^{-1}$), D' ($\sim 1620 \text{ cm}^{-1}$), 2D ($\sim 2700 \text{ cm}^{-1}$) and D + D' ($\sim 2925 \text{ cm}^{-1}$) bands and their Lorentzian line shape reveal the sp^2 crystallinity, doping, local environment of structural defects, strain *etc.* Fig. 1(d) presents the integrated intensity ratios of D, G, 2D ($I_{\text{D}}/I_{\text{G}}$ and $I_{2\text{D}}/I_{\text{G}}$), inter-defect distance (L_{D}) and areal defect density (n_{D}) for each sample. In order to calculate the n_{D} and L_{D} from the $I_{\text{D}}/I_{\text{G}}$ ratio, we have used the empirical relations proposed by Cañado *et al.*⁴⁰ These empirical relations were validated in one of our earlier reports on Au-functionalized GR.³¹

$$L_{\text{D}}^2 (\text{nm}^2) = (1.8 \pm 0.5) \times 10^{-9} \lambda_{\text{L}}^4 \left(\frac{I_{\text{D}}}{I_{\text{G}}} \right)^{-1} \quad (1)$$

$$n_{\text{D}} (\mu\text{m}^{-2}) = \frac{(1.8 \pm 0.5)}{\lambda_{\text{L}}^4} \times 10^{14} \left(\frac{I_{\text{D}}}{I_{\text{G}}} \right) \quad (2)$$

where λ_{L} is the excitation wavelength in nm.^{32,40} The sharp G and 2D bands (intensity ratio $I_{2\text{D}}/I_{\text{G}} = 6$) and the absence of the D band in GR is significant for perfect sp^2 crystallinity with monolayer coverage of graphene. The surface modification of GR with Au NPs gives rise to the appearance of a broad D band and a considerable red shift in the 2D band due to the in-plane lattice strain in the graphene layer, which arises from the interaction of GR with Au NPs. Note that no considerable change in the Raman shift and full width at half-maxima (FWHM) in the G band was observed after Au deposition on GR, which implies a noncovalent interaction of Au NPs with GR. Strong Raman features of the D and D' bands in the DGR sample are a representation of various intrinsic defects (vacancy defects, line defects *etc.*) on the

Table 1 Details of the graphene hybrid samples studied in this work

Sl. no	Description of the graphene hybrid samples	Sample code
1.	Defect-free CVD graphene	GR
2.	Defective CVD graphene	DGR
3.	Graphene oxide	GO
4.	Au sputtered on GR, RTA treated	GRAu
5.	Au sputtered on DGR, RTA treated	DGRAu
6.	Au sputtered on GO, RTA treated	GOAu

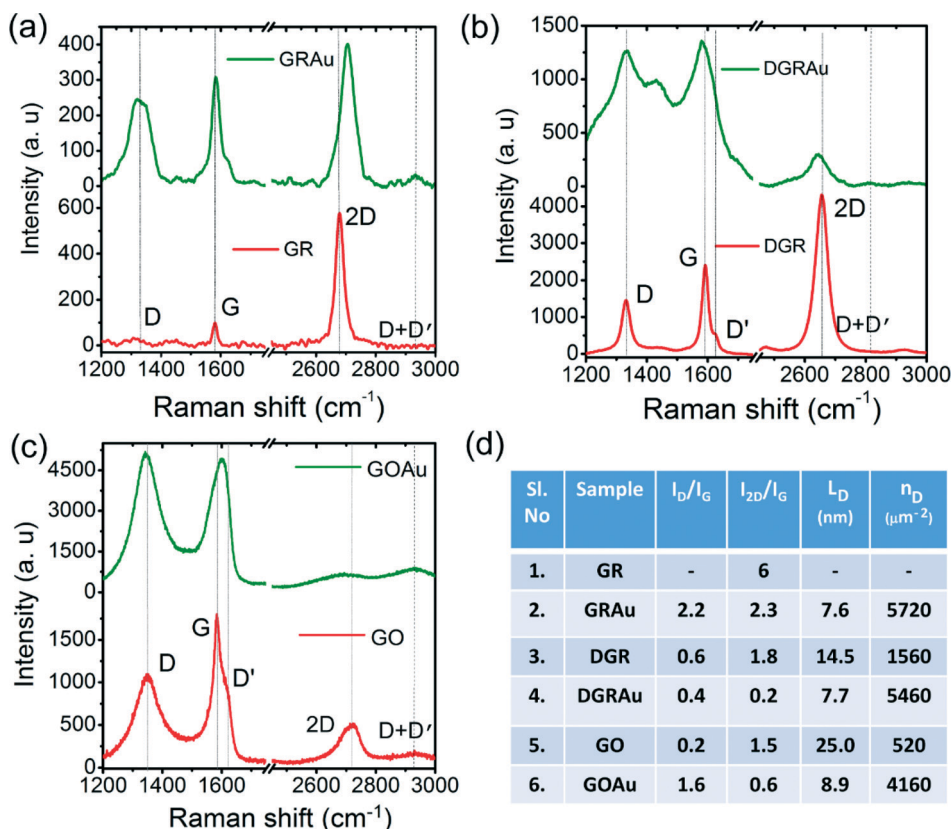


Fig. 1 Characteristic Raman features of CVD graphene (GR) and graphene oxide (GO) before and after Au functionalization: (a) GR, (b) DGR and (c) GO. The structural defects, disorder due to functional groups and defect density are estimated from the integrated intensity ratios of I_D/I_G and I_{2D}/I_G , which are calculated from the Lorentzian line shape fitting. (d) Summary of the ratio of Raman intensities I_D/I_G and I_{2D}/I_G and the calculated inter-defect distance (L_D) and defect density (n_D) for different samples.

graphene layer that form during the CVD growth process (see Fig. 1(b)). The site selective defect mediated strong interaction of Au NPs with the DGR layer is depicted by the distinct Raman features that are different from the Raman spectrum of GRAu, based on the broad line shape of the D and G bands and deterioration of the 2D band ($I_{2D}/I_G = 0.2$) in the case of DGRAu. Note that both G and 2D bands show a red shift after Au functionalization of DGR, which is significant for the p-doping of graphene. A new Raman band at 1430 cm^{-1} represents the interaction of Au NPs at the edge sites of the graphene layer.³² In the case of GO, it shows a broad Raman feature consisting of D, G and 2D bands due to the in-plane oxygenated functional groups, as shown in Fig. 1(c). The enhancement in the intensity ratio I_D/I_G indicates the interaction and functionalization of GO with Au NPs. In addition, there is a decrease in inter-defect distance (L_D) and increase in defect density (n_D) after physical functionalization with Au (see Fig. 1(d)) for all the samples. This clearly revealed that there is a strong interaction between the Au NPs and the defective sites of GO that leads to clustering of Au atoms at the defect sites as well as at the functional groups.³²

Raman mapping was performed on the DGR and DGRAu samples for the well-known D, G and 2D bands for the surface coverage and uniformity of the GR layer as well as the interaction of Au on top of graphene. Fig. 2(a–c) represent

the Raman mapping images scanned with 514.5 nm excitation in an area of $20 \times 20\ \mu\text{m}^2$, which show a full coverage of SLG as evident from the prominent 2D band at $\sim 2700\text{ cm}^{-1}$.^{32,41} The graphitic G band at $\sim 1595\text{ cm}^{-1}$ signifies the sp^2 hybridization of carbon atoms and is assigned to the E_{2g} (high) mode of in-plane C–C stretching vibration. The ratio of intensities of the 2D and G bands I_{2D}/I_G is ~ 1.00 , which indicates the presence of SLG and FLG. The high intensity of the defect band D at $\sim 1350\text{ cm}^{-1}$ implies the presence of point and line defects in DGR. Some of the defects might have been introduced during the wet transfer process of graphene onto the Si/SiO₂ substrate. Fig. 2(d and e) represent the Raman mapping of the DGRAu plasmonic hybrid structure for D and G bands. Note that the spatial Raman mappings of DGRAu were taken for the $5 \times 5\ \mu\text{m}^2$ area. Fig. 2(f) shows the ratio of the integrated intensity of D to G bands (I_D/I_G), which is very important for calculating n_D and L_D . Raman mappings of D and G bands in DGRAu clearly reveal the role of in-plane defects in graphene for the surface dewetting and clustering of Au atoms to form Au NPs. The intense circular spots observed in Fig. 2(f) indicate additional defects, which may have been introduced during the sputter deposition of Au film on the graphene layer.

The chemical composition of sp^2/sp^3 carbon and the presence of various oxygenated functional groups and Au were

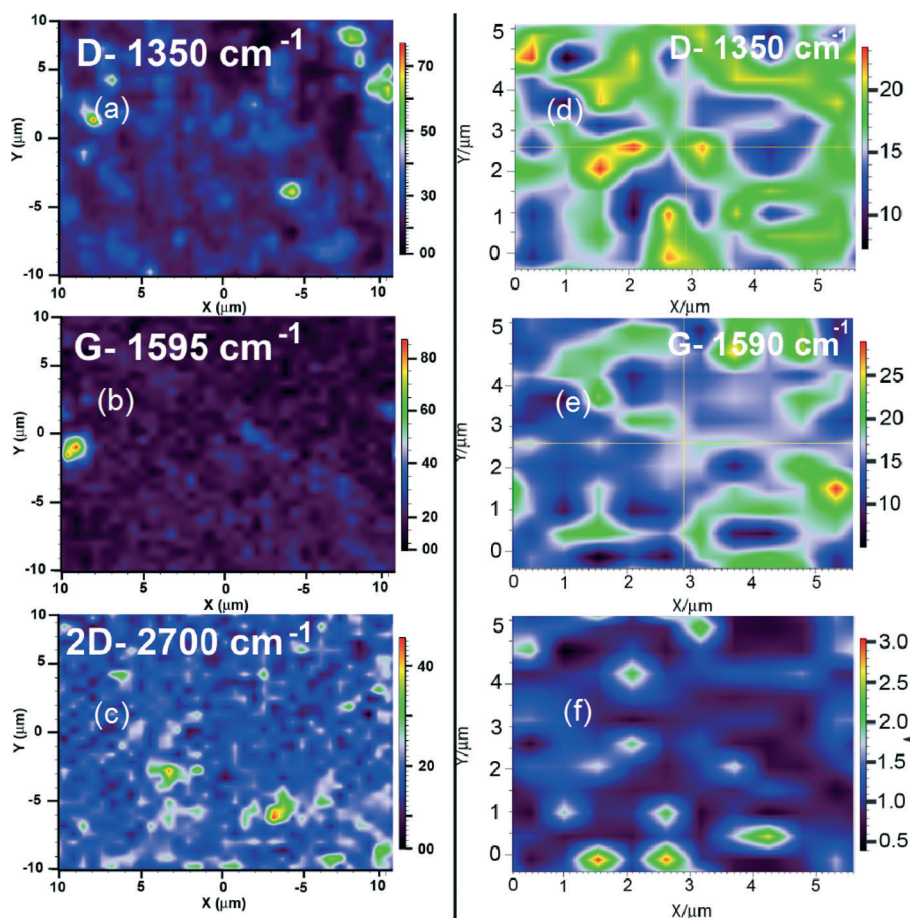


Fig. 2 (a–c) Spatial Raman mappings of pristine CVD graphene (DGR) for D, G and 2D bands, respectively, which indicate the presence of BLG and FLG (reprinted with permission from *J. Phys. Chem. C*, 2014, **118**, 13833. Copyright (2014) American Chemical Society). (d–f) Raman mappings of DGRAu hybrid for D band and G band and corresponding I_D/I_G ratio, respectively. Note that the Raman mappings of GR and DGRAu are recorded with $20 \times 20 \mu\text{m}^2$ and $5 \times 5 \mu\text{m}^2$ area, respectively, using 514.5 nm laser excitation.

identified from the XPS and FTIR spectra, as shown in the ESI† (Fig. S1). The commonly observed oxygen functional group in GO is the OH group and various conjugated CO functionalities covalently bonded within the sp^2/sp^3 carbon domains.³⁹

4.2. HRTEM studies

The morphological features of pristine and Au-functionalized GR, DGR and GO were investigated from the HRTEM image to assess the homogeneity, number of layers, structural defects on the basal plane, edges and the interaction of Au NPs at the defect sites. Fig. 3(a) shows the TEM image of GR suspended on a TEM Cu grid and the corresponding selective area electron diffraction (SAED) pattern showing the hexagonal lattice spots of sp^2 hybridized carbon atoms. The arrows indicate the residual PMMA particles and formation of wrinkles on the graphene basal plane that are formed during the wet transfer process of graphene from the Cu foil to the TEM grid.¹⁶ The SAED pattern was taken at several locations on the GR layer and reveals perfect sp^2 hybridization without

any structural defects. Further, the spatial distribution of in-plane and edge defects is illustrated in Fig. 3(b) for the DGR sample that shows the vacancy-type defects and extended line defects, which are formed during the CVD growth. The cross section of the graphene layers in GO is shown in Fig. 3(c) that shows the distribution of layers and the lattice distortions in the GO sheets. The left and right insets show the GO layer and corresponding SAED pattern of Fig. 3(c), respectively. The shaded portions may be due to the oxygenated functionalities and disorder in the layers of GO. The multiple electron diffraction spots arise from the GO basal plane, as shown in the inset of Fig. 3(c). The average number of graphene layers present in the GO sample is nearly 10. However, oxygenated single layer and few layer graphene may have absorption and photoluminescence spectra similar to those of multilayer GO.³⁹

Further, the surface modification of defect-free and defective graphene and GO functionalized with the Au NPs was investigated by suspending them on a TEM Cu grid. Fig. 3(d) represents the TEM image of GR after Au NP functionalization and the corresponding HRTEM image

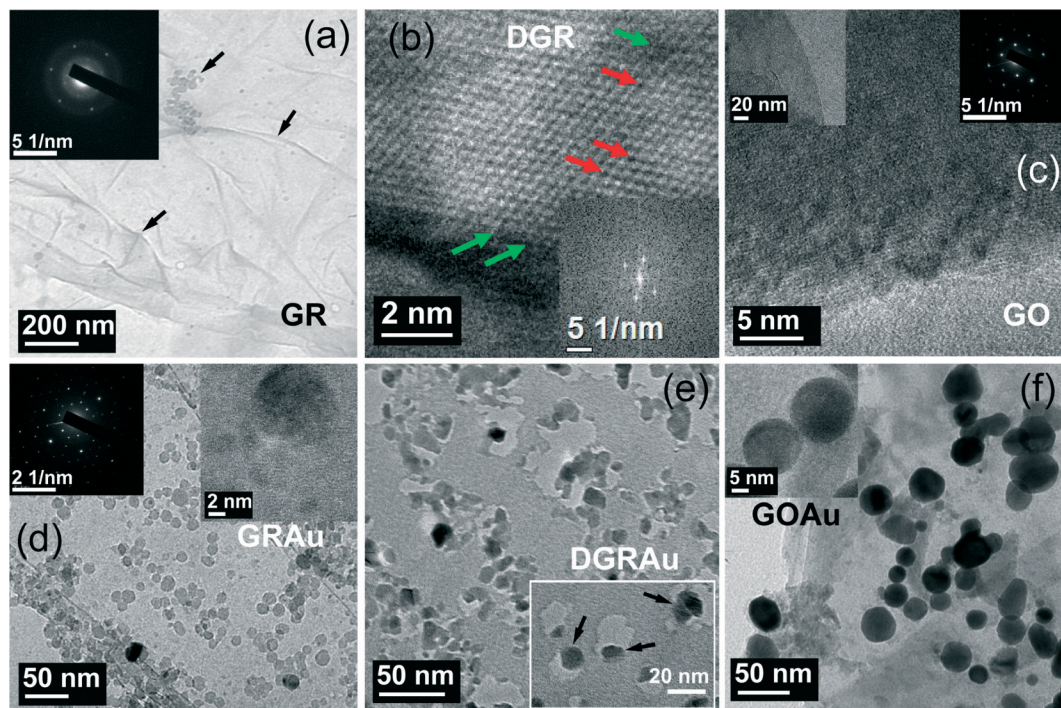


Fig. 3 TEM images of GR and GO before and after Au functionalization: (a) GR suspended onto a copper TEM grid. The inset shows the corresponding SAED pattern representing a single layer graphene. The arrows indicate the formation of wrinkles and residual PMMA particles on the graphene layer during the wet transfer process. (b) HRTEM image of DGR showing various intrinsic defects (edge, line and point defects represented by the arrows). The inset shows the IFFT image exhibiting the hexagonal diffraction spots. (c) Cross section of the multilayer GO sheets. The inset shows a top view of the GO plane and corresponding SAED pattern with hexagonal lattice spots of multilayer graphene. (d) TEM image of GR after Au functionalization. The insets show the corresponding HRTEM image of a single Au NP and graphene lattice and the SAED pattern. (e) TEM image of the site selective functionalization of Au NPs at defect sites of DGR; the inset shows a magnified image of Au NPs at in-plane vacancy sites of graphene. (f) TEM image of Au NP functionalized GO surface. Nearly uniform spherical Au NPs with an average diameter of ~ 20 nm are shown. The inset shows the HRTEM image of Au NPs and the GO interface.

(inset) shows a single Au NP and graphene lattice. The SAED pattern of the GRAu NP hybrid is shown in the upper left inset of Fig. 3(d). Fig. 3(e) shows the TEM image of suspended graphene and Au NPs attached selectively at vacancy sites of DGR and the inset shows a magnified image of Au NPs at in-plane vacancy sites of graphene. The spherical Au NPs are attached on the surface of the GO basal plane, as shown in the TEM image in Fig. 3(f). The HRTEM image shows a lattice pattern of Au NP functionalized with GO (inset). Note that the average size of Au NPs in the case of GRAu and DGRAu is found to be ~ 10 nm, whereas in GOAu it is ~ 20 nm. Thus, the sizes of Au NPs are larger on GO as compared to that on GR and DGR. The possible reason for the difference in the evolution of Au clusters on the CVD graphene and GO surface during the sputter deposition is the chemically and mechanically inert nature of the CVD graphene surface, while in the case of GO most of the in-plane graphene is functionalized with epoxy and C–O related functional groups. Since the CVD graphene mostly has point defects/vacancy clusters on the basal plane and the defect density is much less compared to that of the chemically prepared GO, the size of the Au clusters on the graphene layer is less than that on the GO. Due to the large density of defects and the presence of extended de-

fects in GO prepared by the harsh chemical method, the size of the Au NPs are expected to be larger in the case of GO.

4.3. Optical absorption studies

Optical absorption measurements were carried out on pristine CVD graphene and GO in order to understand the effect of surface functionalities and intrinsic defects on the UV-visible absorption of graphene with/without functionalization with Au NPs. Comparison of the absorption spectra from GR, DGR and GO coated on the quartz substrates is shown in Fig. 4(a). It is evident that the GR is completely transparent over the entire range of the UV-visible-NIR wavelength region as compared to the GO sample that shows considerable absorption in the visible region. The absorption spectrum of DGR looks almost identical to that of GR, though it contains the structural defects on the basal plane and at the edges (see the HRTEM image, Fig. 3(b)). GO shows a broad UV-vis absorption band with a peak at ~ 250 nm due to the stacking of various in-plane and edge oxygenated functional groups corresponding to the defect induced intermediate energy states (sub-bands), *i.e.*, transition from $n-\pi^*$ states.^{1,11} Fig. 4(b) represents the comparison of the absorption spectra

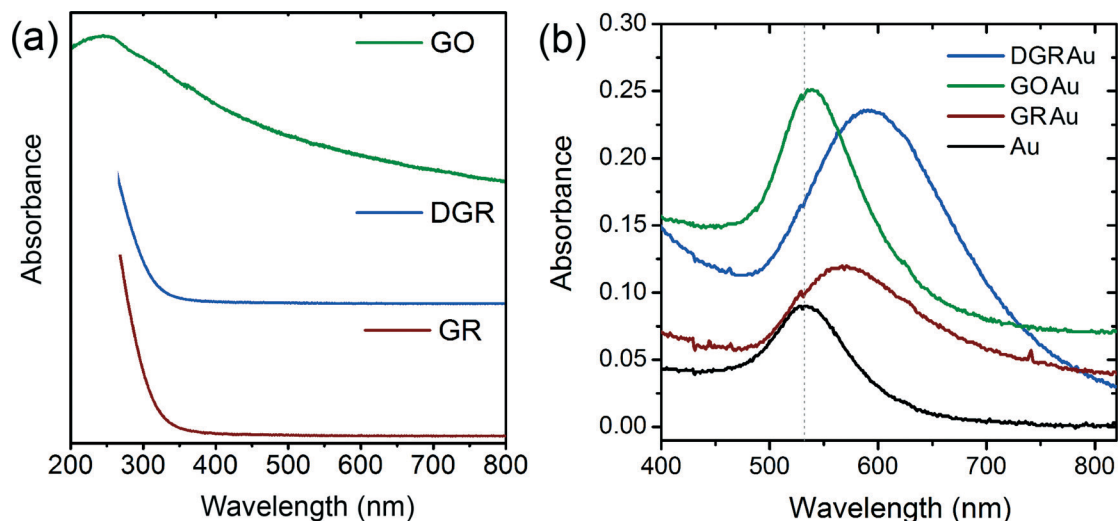


Fig. 4 (a) Optical absorption spectra of GR, DGR and GO transferred onto a quartz substrate. (b) Optical absorption spectra of GR and GO after physical functionalization with Au NPs. A strong surface plasmon resonance absorption peak was found in all the samples.

of Au NPs and Au-functionalized GR, DGR and GO coated on quartz substrates. Au NPs shows a strong SPR absorption band centred at 532 nm in the visible region. The SPR peak positions in the case of GRAu, DGRAu and GOAu were identified at 570, 590 and 540 nm, respectively. It is evident from the absorbance data that DGRAu and GOAu samples show stronger absorption than bare Au NPs due to the strong plasmonic coupling between the DGR/GO and Au NPs. This enhanced absorption can play a significant role in the enhanced photocatalytic reaction (discussed later). Note that there is a large red shift in the SPR band in the case of GRAu and DGRAu, whereas GOAu shows only a small red shift. This is due to the overall increment in the refractive index due to the surrounding dielectric medium of Au NPs in GRAu, DGRAu and GOAu samples.⁴² However, in our samples, the red shift and broadening of the Au plasmon band points to the defect-mediated strong interaction of Au NPs with the graphene basal plane.³² The diffusion of Au clusters/atoms in

graphene⁴³ and formation of longer Au–C bonds⁴⁴ are believed to cause the broadening of the SPR absorption band in the present case. The insignificant change in line width and peak position of the Au plasmon peak in GOAu may be due to the weaker interaction and functionalization of Au NPs at the oxygenated functional groups.⁴⁵

4.4. Visible light photo-degradation performance studies

The photocatalytic performance of different graphene–Au plasmonic hybrid catalysts was evaluated from the efficiency of degradation of an aqueous MB organic dye solution under visible light irradiation (390–730 nm). Fig. 5 represents the schematic process of the dispersion of plasmonic graphene photocatalyst in aqueous MB solution and measurement of the absorption spectra of MB at regular time intervals (every 15 min) under exposure to visible light up to 2 h. We measured the absorption spectrum of irradiated blank MB as well

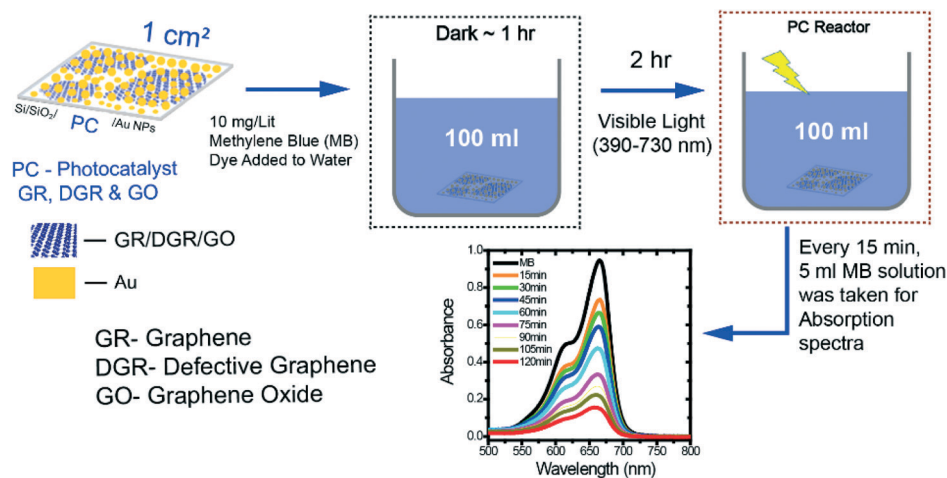


Fig. 5 Schematic of the photocatalysis experiment with graphene–Au plasmonic hybrids.

as catalyst loaded (pristine GR and GRAu) MB solution, maintaining identical reaction conditions. As compared to the pristine GR and GO, a significantly improved performance of the visible light photodegradation of MB was observed in the presence of DGRAu and GOAu samples, as shown in Fig. 6(a and b). Fig. 6(c) represents a bar diagram of the photodegradation performance for all the pristine and GRAu plasmonic hybrid catalysts. It is clear that DGRAu, GO

and GOAu show superior photodegradation performance with visible light with efficiencies of 67%, 70% and 85%, respectively, after irradiating the sample for 120 min. Note that since we used a thin film of the catalysts, the sample area exposed to the dye is much less compared to the size/volume of the container/dye solution and this resulted in the moderate efficiency of degradation. Much higher degradation efficiency could be expected if larger area catalyst samples are prepared and exposed to visible light uniformly.

Fig. 7(a) illustrates the fraction of degradation C_t/C_0 as a function of the irradiation time for different samples. Here, C_0 and C_t denote the concentration of MB solution before and after irradiation for a period t , respectively, when the adsorption-desorption equilibrium was achieved. The degradation of MB was considered as a pseudo-first-order reaction, expressed by the rate equation $\ln(C_0/C_t) = kt$, where k is a first-order rate constant.^{13,15,46} The value of k is calculated from the logarithmic plot of C_t/C_0 as a function of the irradiation time (t) using a linear fit, as shown in Fig. 7(b). Note that the symbols represent the experimental data and the solid lines correspond to the fitted data for the first-order rate equation. Fig. 7(c) represents a comparison of the k values for different catalysts and it clearly shows a dramatic improvement in the rate constant k after Au functionalization of DGR and GO. On the other hand, no significant enhancement was observed in the case of pristine GR and GRAu catalysts. The higher photocatalytic efficiency displayed by DGRAu and GOAu photocatalysts than the pristine samples (without Au functionalization) having the same size/density is likely to be caused by the strong bonding of plasmonic metal NPs functionalized at defect sites in DGR and oxygen functional groups in GO, respectively, which results in the efficient charge transfer and charge separation. We estimated a rate constant of 6.87×10^{-4} and $8.26 \times 10^{-4} \text{ min}^{-1}$ for Au functionalized DGR and GO, respectively. Note that due to the use of a thin film substrate, the sample area of the photocatalyst interacting with the MB solution is much small compared to the total volume of the MB solution. This may have resulted in a lower rate constant. However, these results are significant considering the visible light catalytic efficiency of DGRAu and GOAu.

Based on the results of the photodegradation of MB and the rate of its degradation (rate kinetics) by graphene and Au-functionalized graphene photocatalysts, we can comment on the mechanism of photocatalysis. One essential requirement for effective photocatalytic degradation of an organic molecule is the formation of good interfacial contact between dye and catalyst. The strong π - π interaction between MB and GO/DGR strongly holds them together. Interestingly, GO shows much better degradation performance as compared to DGR due to the active participation of attached functional groups, -OH, -OOR *etc.*, present on the basal plane of GO in the photocatalysis. These functional groups directly influence the photocatalytic efficiency. Since GO possesses a semiconducting nature, charge separation is more efficient than that in graphene. On the other hand, DGR has mainly defect sites

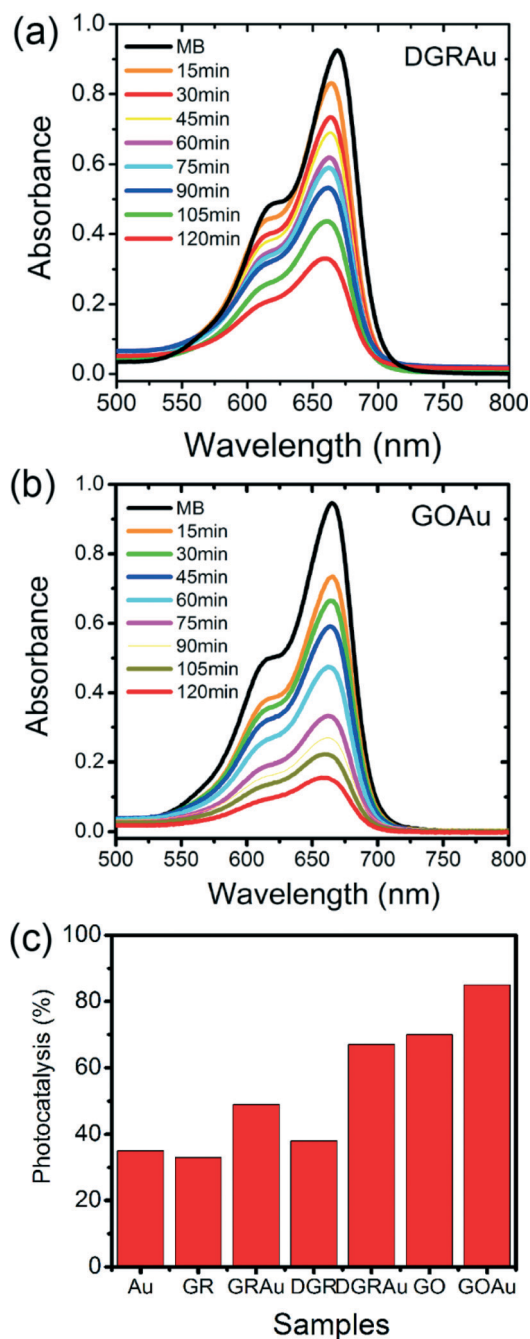


Fig. 6 Change in absorbance of MB during the visible light photocatalytic degradation in the presence of (a) DGRAu and (b) GOAu plasmonic hybrid catalysts. (c) A bar diagram showing the comparison of the photodegradation performance of different catalysts.

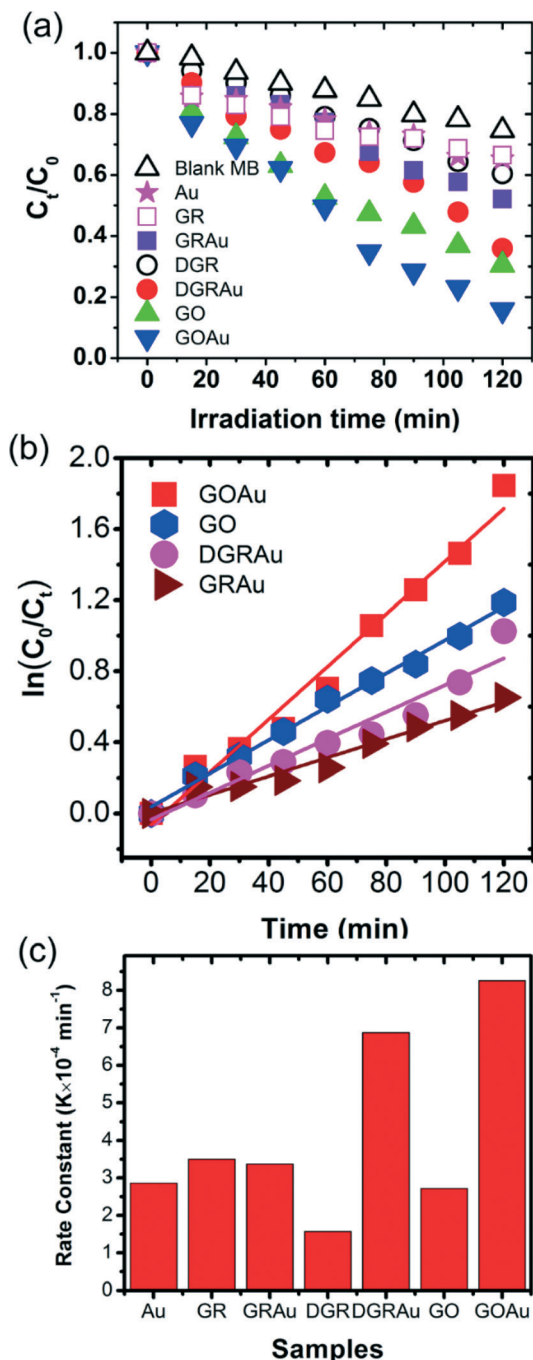


Fig. 7 (a) Visible light photocatalytic activity (C_t/C_0) of graphene and Au functionalized graphene catalytic substrates in MB solution as a function of irradiation time. (b) Log plot of photodegradation of MB as a function of irradiation time; the corresponding first-order rate constant (k) was calculated from the linear fitting. The symbols represent the experimental data and solid lines correspond to the fitted line. (c) A comparison of the rate constants before and after Au physical functionalization of different graphene catalysts for visible light irradiation.

(e.g. carbon vacancies, extended defects) where charge trapping can occur. It appears that the contribution of intrinsic defects to photocatalysis is less compared to that of the functional groups. DGR has a more improved performance than

GR because GR has negligible defect sites or too few active functional groups necessary for photocatalysis.

One of the main drawbacks of graphene in photocatalysis is its poor ability to absorb visible light. GO shows some absorption in the visible region, while GR and DGR are ineffective in doing so. One of the important reasons for using plasmonic Au nanoparticles on graphene surface is to utilize the visible light of the solar spectrum for the enhancement of photocatalysis. Under visible light illumination, surface plasmon resonance excitation of Au nanoparticles can build up a large photon intensity and high concentration of energetic electrons on its surface. In the hybrid system with graphene, these photon energy and electrons are accumulated at the Au-graphene interface. The Au NPs as the electron reservoir as well as the photoexcitation of electrons on the Au surface can easily undergo plasmon-mediated charge transfer from Au nanoparticles to the graphene nanosheet. However, the charge transfer interaction between the adsorbed Au nanoparticles and the graphene nanosheet depends on how strongly the Au nanoparticles are bonded with the graphene nanosheet, which is evidently different in DGRAu and GOAu.^{47–49} The defect sites in DGR are mostly carbon vacancies, which provide nucleation sites for Au migration and clustering. Defective graphene with carbon vacancy sites can provide C-dangling bonds for the attachment of Au atoms on top of the nanosheet. The Au-C bond can form by the interaction of the d-shell electron of Au with the sp^2 dangling bonds of carbon atoms of defective graphene. This strong interaction can provide stable support for Au NPs and facilitate efficient charge transfer from Au NPs to the graphene sheet through Au-C linkage. Au atoms on GO will find the edge functional groups such as epoxy, carboxy, and hydroxyl functional groups to form Au-C and Au-O linkages and stabilize the Au NPs and contribute to plasmon-mediated charge transfer interaction. The defect-free graphene nanosheet is chemically inert and the added Au atoms may be highly mobile on the graphene sheet and become unstable. Thus, there may be negligible interaction between GR and Au for effective plasmon-mediated charge transfer in the defect-free graphene hybrid system.

The photocatalytic activity of pristine Au NPs and the MB blank is also examined for comparison, and they exhibit very weak efficiency in MB degradation over 2 h of irradiation. Au functionalization results in the enhancement of photocatalytic activity in DGR and GO by ~ 2.5 times. Based on these observations, we can provide a mechanistic view of the photocatalytic activities happening on Au-decorated DGR and GO nanosheets, and this is represented as a schematic in Fig.8. Fig. 8(a and b) represent the atomic model of the DGRAu and GOAu systems, depicting the physical functionalization of Au clusters/NPs at the defect sites and oxygenated functional groups, respectively. Note that these models are simulated using the Atomic Tools Kit (Quantumwise, ATK 11.8.2). Fig. 8(c) depicts the energy band diagram of the graphene-Au

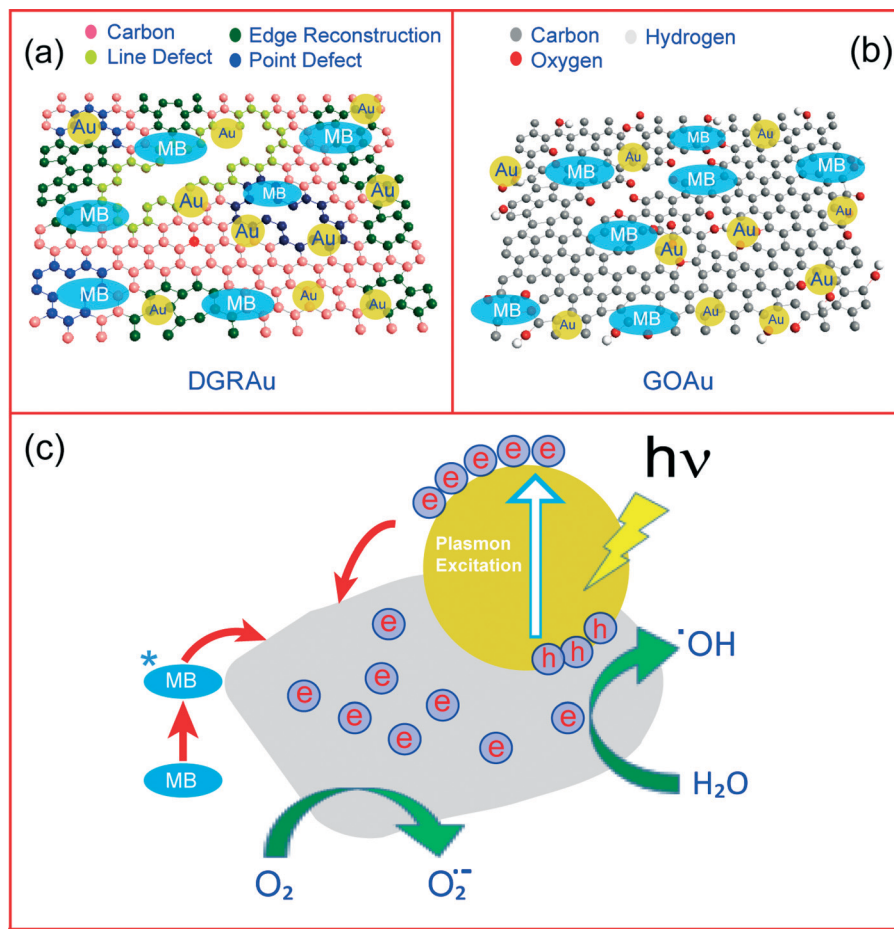


Fig. 8 Atomic model of the physical functionalization of graphene/GO with Au NPs: (a) DGR and (b) GO. (c) Proposed mechanism of enhanced visible light photocatalysis in DGRAu and GOAu hybrid photocatalysts.

plasmonic hybrid system, which illustrates the charge transfer mechanism during visible light excitation. Au NPs can play a dual role in the enhancement of photocatalytic activity of DGRAu and GOAu hybrids. Firstly, Au NPs as a reservoir of electrons can transfer electrons to DGR or GO. Secondly, excitation of Au nanoparticles at its surface plasmonic band will cause intraband electronic transition in Au and these excited electrons will migrate to the surface.⁵⁰ The accumulated electrons on the Au surface will be transferred to the graphene nanosheet through the Au–C linkage with DGR and GO nanosheets, thereby triggering the photocatalytic activities. Because of the extended π conjugation, once accumulated on graphene nanosheet the electrons will be transported far away from the contact of Au–graphene interface. Au nanoparticles will be left with positive holes on their surface after electron release to GR. These holes on Au will recombine with other photoexcited electrons in Au or react with the adsorbed H_2O to form hydroxyl radical ($\cdot\text{OH}$). The electrons on the graphene nanosheet will react with adsorbed O_2 molecule and form superoxide radical ($\text{O}_2^{\cdot-}$). These reactive oxygen species ($\text{O}_2^{\cdot-}$ and $\cdot\text{OH}$) will finally interact with the adsorbed MB molecule and decompose it.

5. Conclusion

In conclusion, a new class of visible light photocatalysts is fabricated by using CVD graphene and GO based transition metal plasmonic hybrids through a physical functionalization approach using RF magnetron sputtering followed by a RTA treatment. We implemented graphene, GO and GRAu plasmonic hybrids for efficient visible light photocatalysis and achieved a strong 85% photodegradation of MB dye molecules using thin films of catalysts. Defect-mediated efficient functionalization and easy charge transfer at the DGRAu interface is believed to be responsible for the enhanced visible light photocatalytic performance of the DGRAu and GOAu NP hybrids. These results are significant and open up pathways for the development of next-generation visible light photocatalysts using graphene and other 2D nanomaterials through physical functionalization with transition metal NPs.

Acknowledgements

We acknowledge the financial support from CSIR (Grant No. 03(1270)/13/EMR-II) and DEITY (Grant No. 5(9)/2012-NANO(Vol.II)) in carrying out part of this work. BC thanks IIT

Guwahati for providing an institute postdoctoral fellowship. We thank Jitendra Kumar for help in the simulation of structural defects in graphene using the ATK toolkit. We thank Dr. Sandip Dhara, IGCAR, Kalpakkam, for the support with the Raman mapping data.

References

- 1 M. J. Benotti, R. A. Trenholm, B. J. Vanderford, J. C. Holady, B. D. Stanford and S. A. Snyder, *Environ. Sci. Technol.*, 2009, **43**, 597–603.
- 2 D. A. Keane, K. G. McGuigan, P. F. Ibanez, M. I. Polo-Lopez, J. A. Byrne, P. S. M. Dunlop, K. O'Shea, D. D. Dionysiou and S. C. Pillai, *Catal. Sci. Technol.*, 2014, **4**, 1211–1226.
- 3 M. Ni, M. K. H. Leung, D. Y. C. Leung and K. Sumathy, *Renewable Sustainable Energy Rev.*, 2007, **11**, 401–425.
- 4 P. V. Kamat, *J. Phys. Chem. C*, 2012, **116**, 11849–11851.
- 5 M. A. Fox and M. T. Dulay, *Chem. Rev.*, 1993, **93**, 341–357.
- 6 N. Bao, L. Shen, T. Takata and K. Domen, *Chem. Mater.*, 2008, **20**, 110–117.
- 7 A. McLaren, T. Valdes-Solis, G. Li and S. C. Tsang, *J. Am. Chem. Soc.*, 2009, **131**, 12540–12541.
- 8 J. S. Hu, L. L. Ren, Y. G. Guo, H. P. Liang, A. M. Cao, L. J. Wan and C. L. Bai, *Angew. Chem., Int. Ed.*, 2005, **44**, 1269–1273.
- 9 A. L. Linsebigler, G. Lu and J. T. Yates, *Chem. Rev.*, 1995, **95**, 735–758.
- 10 R. Jiang, B. Li, C. Fang and J. Wang, *Adv. Mater.*, 2014, **26**, 5274–5309.
- 11 V. Subramanian, E. Wolf and P. V. Kamat, *J. Phys. Chem. B*, 2001, **105**, 11439–11446.
- 12 G. Williams, B. Seger and P. V. Kamat, *ACS Nano*, 2008, **2**, 1487–1491.
- 13 N. Zhang, S. Liu, X. Fu and Y. J. Xu, *J. Phys. Chem. C*, 2011, **115**, 9136–9145.
- 14 B. Choudhury, B. Borah and A. Choudhury, *Photochem. Photobiol.*, 2012, **88**, 257–264.
- 15 N. Zhou, L. Polavarapu, N. Gao, Y. Pan, P. Yuan, Q. Wang and Q. H. Xu, *Nanoscale*, 2013, **5**, 4236–4241.
- 16 M. R. Hoffmann, S. T. Martin, W. Choi and D. W. Bahnemann, *Chem. Rev.*, 1995, **95**, 69–96.
- 17 X. Z. Li and F. B. Li, *Environ. Sci. Technol.*, 2001, **35**, 2381–2387.
- 18 Z. Wang, S. Zhao, S. Zhu, Y. Sun and M. Fang, *CrystEngComm*, 2011, **13**, 2262–2267.
- 19 D. M. Schaadt, B. Feng and E. T. Yu, *Appl. Phys. Lett.*, 2005, **86**, 063106.
- 20 N. Zhang, Y. Zhang and Y. J. Xu, *Nanoscale*, 2012, **4**, 5792–5813.
- 21 A. K. Singh, K. Mathew, H. L. Zhuang and R. G. Hennig, *J. Phys. Chem. Lett.*, 2015, **6**, 1087–1098.
- 22 Q. Xiang, J. Yu and M. Jaroniec, *Chem. Soc. Rev.*, 2012, **41**, 782–796.
- 23 Q. Xiang and J. Yu, *J. Phys. Chem. Lett.*, 2013, **4**, 753–759.
- 24 C. Huang, C. Li and G. Shi, *Energy Environ. Sci.*, 2012, **5**, 8848–8868.
- 25 Y. Zhang, N. Zhang, Z. R. Tang and Y.-J. Xu, *J. Phys. Chem. C*, 2014, **118**, 5299–5308.
- 26 W. Gao, M. Majumder, L. B. Alemany, T. N. Narayanan, M. A. Ibarra, B. K. Pradhan and P. M. Ajayan, *ACS Appl. Mater. Interfaces*, 2011, **3**, 1821–1826.
- 27 A. C. Ferrari, F. Bonaccorso, V. Fal'ko, K. S. Novoselov, S. Roche, P. Boggild, S. Borini, F. H. L. Koppens, V. Palermo, N. Pugno, J. A. Garrido, R. Sordan, A. Bianco, L. Ballerini, M. Prato, E. Lidorikis, J. Kivioja, C. Marinelli, T. Ryhanen, A. Morpurgo, J. N. Coleman, V. Nicolosi, L. Colombo, A. Fert, M. Garcia-Hernandez, A. Bachtold, G. F. Schneider, F. Guinea, C. Dekker, M. Barbone, Z. Sun, C. Galiotis, A. N. Grigorenko, G. Konstantatos, A. Kis, M. Katsnelson, L. Vandersypen, A. Loiseau, V. Morandi, D. Neumaier, E. Treossi, V. Pellegrini, M. Polini, A. Tredicucci, G. M. Williams, B. H. Hong, J.-H. Ahn, J. M. Kim, H. Zirath, B. J. van Wees, H. van der Zant, L. Occhipinti, A. Di Matteo, I. A. Kinloch, T. Seyller, E. Quesnel, X. Feng, K. Teo, N. Rupesinghe, P. Hakonen, S. R. T. Neil, Q. Tannock, T. Lofwander and J. Kinaret, *Nanoscale*, 2015, **7**, 4598–4810.
- 28 M. Q. Yang, N. Zhang, M. Pagliaro and Y. J. Xu, *Chem. Soc. Rev.*, 2014, **43**, 8240–8254.
- 29 N. Zhang, M. Q. Yang, S. Liu, Y. Sun and Y. J. Xu, *Chem. Rev.*, 2015, **115**, 10307–10377.
- 30 G. Eda and M. Chhowalla, *Adv. Mater.*, 2010, **22**, 2392–2415.
- 31 C. Mattevi, H. Kim and M. Chhowalla, *J. Mater. Chem.*, 2011, **21**, 3324–3334.
- 32 R. K. Biroju and P. K. Giri, *J. Phys. Chem. C*, 2014, **118**, 13833–13843.
- 33 A. K. Geim and K. S. Novoselov, *Nat. Mater.*, 2007, **6**, 183–191.
- 34 I. V. Lightcap, T. H. Kosel and P. V. Kamat, *Nano Lett.*, 2010, **10**, 577–583.
- 35 S. K. Bhunia and N. R. Jana, *ACS Appl. Mater. Interfaces*, 2014, **6**, 20085–20092.
- 36 P. V. Kamat, *J. Phys. Chem. Lett.*, 2010, **1**, 520–527.
- 37 H. Zhang, X. Fan, X. Quan, S. Chen and H. Yu, *Environ. Sci. Technol.*, 2011, **45**, 5731–5736.
- 38 Z. Xiong, L. L. Zhang, J. Ma and X. S. Zhao, *Chem. Commun.*, 2010, **46**, 6099–6101.
- 39 R. K. Biroju, G. Rajender and P. K. Giri, *Carbon*, 2015, **95**, 228–238.
- 40 L. G. Cançado, A. Jorio, E. H. M. Ferreira, F. Stavale, C. A. Achete, R. B. Capaz, M. V. O. Moutinho, A. Lombardo, T. S. Kulmala and A. C. Ferrari, *Nano Lett.*, 2011, **11**, 3190–3196.
- 41 K. B. Ravi, T. Nikhil, R. Gone, S. Dhara and P. K. Giri, *Nanotechnology*, 2015, **26**, 145601.
- 42 A. Sánchez-Iglesias, E. Carbó-Argibay, A. Glaria, B. Rodríguez-González, J. Pérez-Juste, I. Pastoriza-Santos and L. M. Liz-Marzán, *Chem. – Eur. J.*, 2010, **16**, 5558–5563.
- 43 Y. Gan, L. Sun and F. Banhart, *Small*, 2008, **4**, 587–591.
- 44 H. Wang, Q. Wang, Y. Cheng, K. Li, Y. Yao, Q. Zhang, C. Dong, P. Wang, U. Schwingenschlöggl, W. Yang and X. X. Zhang, *Nano Lett.*, 2011, **12**, 141–144.
- 45 M. Ding, Y. Tang and A. Star, *J. Phys. Chem. Lett.*, 2012, **4**, 147–160.
- 46 A. Houas, H. Lachheb, M. Ksibi, E. Elaloui, C. Guillard and J. M. Herrmann, *Appl. Catal., B*, 2001, **31**, 145–157.

- 47 A. Pulido, M. Boronat and A. Corma, *New J. Chem.*, 2011, **35**, 2153–2161.
- 48 X. Liu, Y. Yang, M. Chu, T. Duan, C. Meng and Y. Han, *Catal. Sci. Technol.*, 2016, **6**, 1632–1641.
- 49 C. Ogata, M. Koinuma, K. Hatakeyama, H. Tateishi, M. Z. Asrori, T. Taniguchi, A. Funatsu and Y. Matsumoto, *Sci. Rep.*, 2014, **4**, 3647.
- 50 P. Wang, B. Huang, Y. Dai and M.-H. Whangbo, *Phys. Chem. Chem. Phys.*, 2012, **14**, 9813–9825.